










RESEARCH ARTICLE | JULY 11 2023

Large ordered moment with strong easy-plane anisotropy and vortex-domain pattern in the kagome ferromagnet Fe₃Sn

Lilian Prodan ; Donald M. Evans ; Sinéad M. Griffin ; Andreas Östlin ; Markus Althaler ; Erik Lysne; Irina G. Filippova ; Sergiu Shova; Liviu Chioncel ; Vladimir Tsurkan ; István Kézsmárki 



Appl. Phys. Lett. 123, 021901 (2023)

<https://doi.org/10.1063/5.0155295>

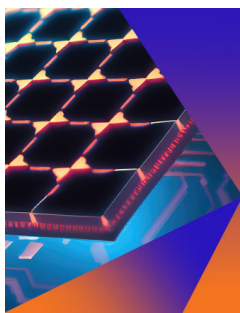


View
Online



Export
Citation

CrossMark



Applied Physics Letters

Special Topic:
Hybrid and Heterogeneous Integration in Photonics:
From Physics to Device Applications

Submit Today

 AIP
Publishing

Large ordered moment with strong easy-plane anisotropy and vortex-domain pattern in the kagome ferromagnet Fe_3Sn

Cite as: Appl. Phys. Lett. **123**, 021901 (2023); doi: 10.1063/5.0155295

Submitted: 19 April 2023 · Accepted: 25 June 2023 ·

Published Online: 11 July 2023



View Online



Export Citation



CrossMark

Lilian Prodan,^{1,a)} Donald M. Evans,¹ Sinéad M. Griffin,^{2,3} Andreas Östlin,⁴ Markus Althaler,¹ Erik Lysne,⁵ Irina G. Filippova,⁶ Sergiu Shova,⁷ Liviu Chioncel,⁴ Vladimir Tsurkan,^{1,6} and István Kézsmárki¹

AFFILIATIONS

¹Experimentalphysik V, Center for Electronic Correlations and Magnetism, Institute of Physics, Augsburg University, D-86135 Augsburg, Germany

²Materials Sciences Division, Lawrence Berkeley National Laboratory, Berkeley, California 94720, USA

³Molecular Foundry, Lawrence Berkeley National Laboratory, Berkeley, California 94720, USA

⁴Theoretische Physik III, Center for Electronic Correlations and Magnetism, Institute of Physics, Augsburg University, D-86135 Augsburg, Germany

⁵Department of Materials Science and Engineering, Norwegian University of Science and Technology (NTNU), 7043 Trondheim, Norway

⁶Institute of Applied Physics, Moldova State University, MD 2028 Chișinău, R. Moldova

⁷Department of Inorganic Polymers, "Petru Poni" Institute of Macromolecular Chemistry, Romanian Academy, 700487 Iasi, Romania

^{a)} Author to whom correspondence should be addressed: lilian.prodan@physik.uni-augsburg.de

ABSTRACT

We report the magnetic anisotropy of kagome bilayer ferromagnet Fe_3Sn probed by the bulk magnetometry and magnetic force microscopy (MFM) on high-quality single crystals. The dependence of magnetization on the orientation of the external magnetic field reveals strong easy-plane magnetocrystalline anisotropy and anisotropy of the saturation magnetization. The leading magnetocrystalline anisotropy constant shows a monotonous increase from $K_1 \approx -1.0 \times 10^6 \text{ J/m}^3$ at 300 K to $-1.3 \times 10^6 \text{ J/m}^3$ at 2 K. Our *ab initio* electronic structure calculations yield the value of total magnetic moment of $7.1 \mu_B/\text{f.u.}$ and a magnetocrystalline anisotropy energy density of -0.57 meV/f.u. ($-1.62 \times 10^6 \text{ J/m}^3$) both being in reasonable agreement with the experimental values. The MFM imaging reveals micrometer-scale magnetic vortices with weakly pinned cores that vanish at the saturation field of $\sim 3 \text{ T}$ applied perpendicular to the kagome plane. The observed vortex-domain structure is well reproduced by the micromagnetic simulations, using the experimentally determined value of the anisotropy and exchange stiffness.

© 2023 Author(s). All article content, except where otherwise noted, is licensed under a Creative Commons Attribution (CC BY) license (<http://creativecommons.org/licenses/by/4.0/>). <https://doi.org/10.1063/5.0155295>

Magnetic compounds with kagome-lattice arrangement of spins have recently attracted much attention due to their unusual magnetic and electronic properties related to the specific topology of their electronic band structures.^{1–6} Recent theoretical and experimental studies have demonstrated that the existence of flat bands, nodal points, and nodal lines appearing close to the Fermi energy significantly affects magnetic,^{7–9} magneto-transport,^{10–14} and magneto-optical^{15,16} properties of kagome materials. They provide an exceptional platform to study electronic band topology and its interplay with magnetic spin and orbital degrees of freedom.

The precise quantification of magnetic anisotropy is the prerequisite to understand the diversity of magnetic spin structures, for which kagome magnets offer a fertile ground.¹⁷ Moreover, the magnetic anisotropy in interplay with the Dzyaloshinskii–Moriya interaction, competing and frustrated exchanges, or dipole–dipole interactions, can affect the spin textures, in the case of conventional domain walls, vortices, and skyrmions.^{18–23} The competition between the magnetic anisotropy and dipole–dipole interaction in the easy-axis magnets can stabilize magnetic bubbles and skyrmions in finite magnetic fields.^{8,19,24,25} The magnets with

easy-plane anisotropy can develop magnetic vortices and antivortices.^{26–30}

In this paper, we investigate the magnetic anisotropy of the itinerant kagome system Fe_3Sn , a member of iron stannides family Fe_xSn_y . Depending on the ratio of $x : y$, i.e., the stacking of kagome layers, these compounds realize different crystal structures and different magnetic ground states. For example, FeSn crystallizes in a structure with $P6/mmm$ space-group symmetry and below 365 K, it is an easy-plane antiferromagnet with ferromagnetic arrangement of spins within each kagome layer.^{31–33} On the other hand, Fe_3Sn_2 crystallizes in the $R\bar{3}m$ symmetry with stacking kagome bi-layers separated by the hexagonal tin layer^{31,34} and it is an easy-axis ferromagnet below 612 K.³⁵ This compound shows skyrmion bubbles at room temperature^{8,24} and a spin reorientation effect, when the easy axis of magnetization gets tilted toward the kagome plane^{34,36–38} at low temperatures. A third type of the kagome stacking is realized in Fe_3Sn , which has a structure of $P6_3/mmc$ symmetry and exhibits ferromagnetic order below 743 K.^{31,34}

The crystal structure of Fe_3Sn is shown in Figs. 1(a) and 1(b). The ab layer consists of a kagome lattice of two sizes of equilateral Fe triangles with Sn atoms in the center of the kagome plane. The unit cell of Fe_3Sn contains two adjacent, laterally displaced kagome layers, separated by half of the lattice constant along the c axis. Early studies reported a ferromagnetic behavior with spin moment oriented along the c axis.^{35,39} In contrast, a recent analysis of magnetic properties of Fe_3Sn by Sales *et al.*⁴⁰ and Fayyazi *et al.*⁴¹ performed on field-oriented polycrystalline powder and very small crystals with a mass of 10 μg , implied predominantly in-plane orientation of the magnetization with the magnitude of easy-plane anisotropy $K_1 = -1.8 \times 10^6 \text{ J/m}^3$ at 300 K.

Here, we report the detailed magnetometry studies and microscopic imaging of the magnetic domain pattern performed on high-quality bulk single crystals of Fe_3Sn . The experimental results are supported by *ab initio* electronic structure calculations and micromagnetic simulations. A typical as-grown Fe_3Sn crystal is shown in the inset of Fig. 1(c). The energy-dispersive x-ray analysis found an excess

of $\text{Fe} \leq 1\%$, indicating a nearly ideal stoichiometry of our samples. Single-crystal x-ray diffraction study revealed the hexagonal $P6_3/mmc$ (#194) space group symmetry and showed no traces of impurity phases. The structural parameters obtained from the single-crystal refinement are summarized in the supplementary material.

The temperature-dependent magnetization measured on heating in 1 T applied along the a axis reveals a steep increase below 750 K indicating the onset of ferromagnetic order, as shown in Fig. 1(c). The Curie temperature of $T_C = 705 \text{ K}$ was extracted from the minimum in the temperature derivative of the magnetization [see the inset of Fig. 1(c)] and is close to the previously reported data for polycrystalline samples.^{31,34}

Figure 1(d) shows the field-dependent magnetization curves, $M(H)$, measured at 2 K for magnetic fields applied along three orthogonal directions. Two directions are in the ab plane, $[1\bar{2}10]$ and $[10\bar{1}0]$, and the hexagonal c axis (equivalently $[0001]$) is the third direction. The magnetization within the ab plane reaches the saturation already at $\sim 1 \text{ T}$. We found that the saturation in the ab plane is reached in nearly the same field for $H \parallel [10\bar{1}0]$ and $H \parallel [1\bar{2}10]$, indicating very small anisotropy in this plane. For fields along the c axis, the saturation takes place at higher fields, above 3 T.

The magnetocrystalline anisotropy constant (K_u) within the ac plane was calculated from the hysteresis curves using an “area method,”⁴² considering the difference of the integrals $\int_0^{M_s} H dM$ for the field orientations along the a and c axes. We obtained the value of $K_u = -1.27 \times 10^6 \text{ J/m}^3$ at 2 K, which decreases to $-0.97 \times 10^6 \text{ J/m}^3$ at room temperature. As pointed out above, and shown in the inset of Figs. 1(d) and S2, the anisotropy in the ab plane is very weak. The sixth-order anisotropy constant calculated from the measurements in the ab plane has the value of $2.3 \times 10^4 \text{ J/m}^3$ at 2 K and $1.8 \times 10^4 \text{ J/m}^3$ at 300 K. Thus, the anisotropy in the ab plane is nearly two orders of magnitude weaker than the anisotropy along c axis, which reveals the easy-plane character of the anisotropy in ferromagnetic Fe_3Sn .

The inset in Fig. 1(d) shows the temperature dependence of the magnetization measured in 7 T. The value of the saturation moment is

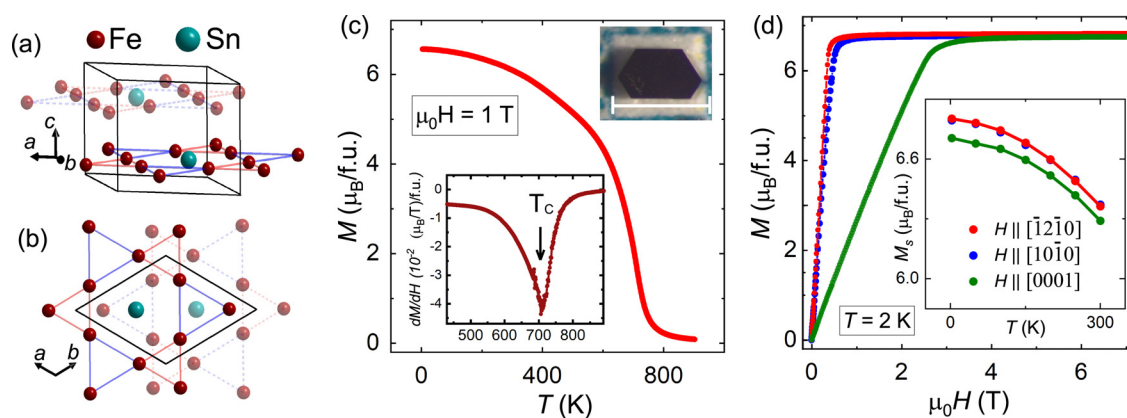


FIG. 1. (a) Schematic representation of the crystal structure of layered Fe_3Sn . Transparent and bold atoms are from different planes. (b) The Fe_3Sn kagome lattices as viewed along the c axis. (c) The temperature-dependent magnetization of Fe_3Sn single crystal measured in 1 T applied along the a axis. The up-right inset shows an as-grown Fe_3Sn single crystal on a millimeter-scale paper. The left-bottom inset shows the first derivative of the temperature-dependent magnetization with the Curie temperature T_C as the location of the minimum. (d) Magnetization curves measured at 2 K in magnetic fields applied in two directions in the ab plane and along the c axis. The inset shows the temperature dependence of the magnetization in 7 T for three crystallographic directions.

2.27 μ_B/Fe at 2 K for field in the ab plane, which is $\sim 2\%$ larger than the saturation value of the magnetization along the c axis. Although this difference is rather small, it cannot originate from the demagnetization effects, since the sample has a circular shape in the ac plane (see Fig. S1) and it is in a single domain state. Additional measurements (not shown here) revealed that this difference is present up to fields as high as 14 T suggesting its relation to orbital effect.

The angular dependence of the magnetization $M(\phi)$ was measured on the same cylindrical-shaped sample with similar demagnetization factors in the ac plane. Figure 2(a) shows the $M(\phi)$ curves measured in different magnetic fields at 300 K. Here, ϕ is the angle spanned by the magnetic field and the c axis [inset of Fig. 2(b)]. In low fields, $M(\phi)$ exhibits a minimum in the field parallel to the c axis and a maximum in the field parallel to the a axis. With increasing magnetic field, the difference between the values of the magnetization in these directions is reduced. In fields above 2 T, $M(\phi)$ changes its functional form. Upon saturation, a local maximum develops also for the field applied along the c axis and a minimum at the intermediate angles. The anisotropy constants were determined from the fit to the $M(\phi)$ curves measured in the fully spin polarized state to avoid complications due to the presence of the magnetic domains.

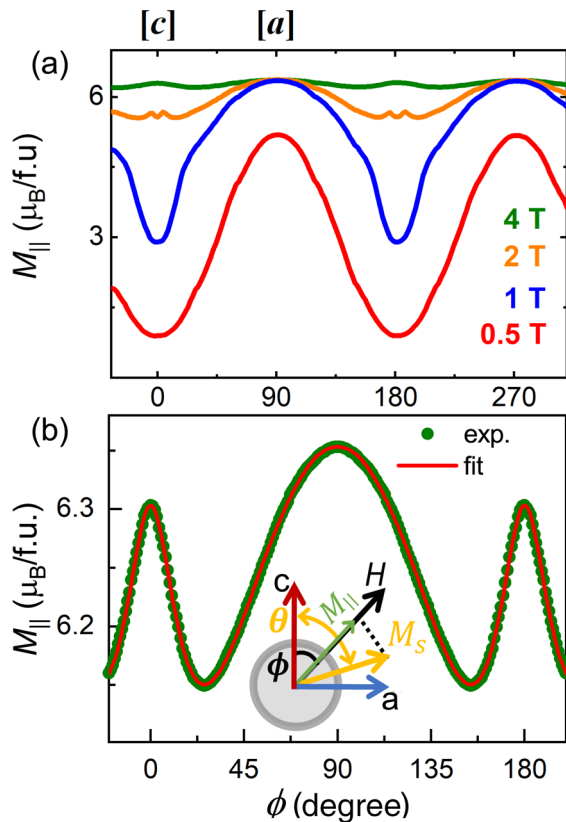


FIG. 2. (a) Angular dependence of the magnetization measured in different fields at 300 K. (b) The fit to the experimental data measured in 4 T. The inset shows a schematic representation of the angular-dependent measurements within the ac -plane. Here, θ is the angle between the magnetization M_s and the c axis, and ϕ is the angle between the c axis and applied magnetic field H .

The angular dependence of the magnetization was fitted based on commonly used phenomenological expression for the magneto-crystalline anisotropy energy (MAE) for a hexagonal ferromagnet,⁴²

$$E_A = K_1 \sin^2 \theta + K_2 \sin^4 \theta + K_3 \sin^6 \theta \cos 6\Psi, \quad (1)$$

where K_1 , K_2 , and K_3 are the first-, second-, and third-order anisotropy constants, respectively. θ is the angle spanned by the magnetization with the c axis, while Ψ denotes the angle between the projection of the magnetization to the ab plane and the a axis. In our fitting, the K_3 term is neglected, since our data show that the in-plane anisotropy is less than 2% of the total magnetic anisotropy, as already mentioned.

By minimizing the total energy per unit volume described as $E = E_A + E_Z$ (where E_Z is the Zeeman energy), one can derive the fitting formula for the angular-dependent magnetization with K_1 and K_2 as fit variables,

$$\sin 2\theta(K_1 + 2K_2 \sin^2 \theta) = -H \sqrt{M_s^2 - M_{\parallel}^2}, \quad (2)$$

where M_{\parallel} is the projection of M_s on the applied field, which is measured in the experiment [see inset of Fig. 2(b)], and H is the applied magnetic field (4 T, single domain state).

The fit to the angular-dependent magnetization using Eq. (1) describes well the angular dependence of $M(\phi)$ well over the whole angular range except for the immediate vicinity of the c axis, where it overshoots the experimental data (not shown here). From the fit, we derived the value of the first anisotropy constant $K_1 = -1.46 \times 10^6 \text{ J/m}^3$ at 2 K, which is comparable with $K_1 = -1.34 \times 10^6 \text{ J/m}^3$ determined by the Sucksmith–Thompson (S–T) method (see below).⁴³ The experimentally observed difference of M_s for fields parallel and perpendicular to the c axis indicates an anisotropy ($\sim 2\%$) of the g -tensor, i.e., imply orbital contributions to the magnetization. Here, it is necessary to notice that if the g -tensor anisotropy is completely negligible, the magnetization should point parallel to the applied field in the high-field limit; hence, θ in Eq. (1) and ϕ in Fig. 2(b) would become identical.

To account for the observed anisotropy of the saturation magnetization, we used the approach developed by Alameda *et al.* and Bolyachkin *et al.*^{44,45} (described in the supplementary material). This fit [red curve in Fig. 2(b)] improves the description of the experimental data significantly for angles close to the c axis. By introducing corrections for the angular dependence of the saturation magnetization, the amplitude of the first anisotropy constant K_1 decreased by about 8% and K_2 by about 50%. Figure 3(a) summarizes the temperature dependence of the anisotropy constants K_1 and K_2 , as determined by two independent methods: (a) from the fits to the angular dependence of the magnetization measured in 4 T (marked as the R method) and (b) calculated from the magnetization curves along the c axis, following the modified (S–T) method, which considers the anisotropy of the saturation magnetization.⁴⁵ Both methods yield very close values of K_1 ($K_1 = -1.08 \times 10^6$ and $-1.01 \times 10^6 \text{ J/m}^3$ at 300 K), which shows a monotonous increase with decreasing temperature, and at 2 K, the values of -1.35×10^6 and $-1.34 \times 10^6 \text{ J/m}^3$ for R and S–T methods are obtained, respectively. These results are in contrast to the non-monotonous temperature-dependent behavior of the anisotropy reported by Fayyazi *et al.*⁴¹ On the other hand, the second-order anisotropy constant, K_2 , being positive shows weak temperature dependence and is by approximately one order of magnitude lower

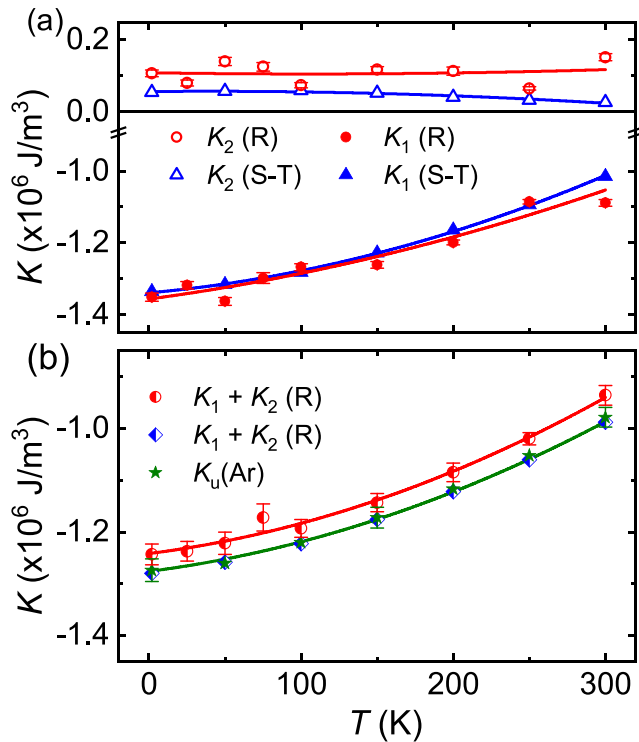


FIG. 3. (a) Temperature-dependent anisotropy constants K_1 and K_2 as determined from the angular dependence of the magnetization (R) and by the Sucksmith-Thompson (S-T) methods. (b) The magnetocrystalline anisotropy constant K_u , determined by the “area method” (Ar) is plotted together with $K_1 + K_2$ taken from panel (a). Lines are guides to the eye.

than K_1 . At 300 K, we obtained $K_2 = 1.5 \times 10^5$ and $2.7 \times 10^4 \text{ J/m}^3$ using the R and S-T methods, respectively.

To validate our calculation of the magnetocrystalline anisotropy in Fe₃Sn, in Fig. 3(b), we compare the sum of $K_1 + K_2$, as determined using the R and the S-T methods, with the anisotropy constant K_u , as calculated using the “area method” (Ar). The values obtained by the three methods agree within 4% at all temperatures. The reason for the difference in the values of $K_1 + K_2$ for these methods is mainly related to different values of K_2 . The source of error of K_2 constant is unclear and may be related to different data-sets for fitting: high-field magnetization data in the saturated state in the R method and low-field data in the S-T method. However, the value of K_2 derived from the R method should be taken with precaution because of larger experimental error due to nonlinear extension of the rotator spring and change of its elasticity with lowering temperature.

The density functional theory (DFT) self-consistent computations reveal that in the ferromagnetic ground state, the preferable magnetization direction lies within the *ab*-plane. In the ferromagnetic ground state, the values of Fe spin/orbital moments are of about $2.31/0.07 \mu_B$ and the induced anti-parallel spin moment on Sn-sites is of about $0.12 \mu_B$. The total magnetic moment per formula unit is $7.1 \mu_B/\text{f.u.}$ and is in good agreement with the experiment. In addition, our calculated MAE by comparing the energy of the in-plane and out-of-plane spin

axes is of about -0.57 meV/f.u. ($-1.62 \times 10^6 \text{ J/m}^3$), consistent with our experiment.

The presented magnetization data demonstrate that our bulk crystal behaves as an easy plane ferromagnet. We used magnetic force microscopy (MFM) to image the local magnetic textures on an as-grown *ab*-plane. The contact mode topography image, Fig. 4(a), shows that the surface is largely flat and any changes in magnetic texture are likely to originate from the magnetic order. Figure 4(b) shows a representative MFM image of the virgin zero-field magnetic state. The most striking features are the discontinuities at the center of lines of converging contrast, which are signatures of vortex cores: The origin of the contrast is analyzed in the micromagnetic section below.

To confirm that the microstructure represents the bulk behavior, we apply the saturation magnetic field of 3 T, perpendicular to our sample surface. Figure 4(c) shows that the sample has reached a mono-domain state, as expected from the bulk data. While Fig. 4(c) shows that there are a few remaining areas of magnetic contrast, these correlate with the changes in the topography seen in Fig. 4(a), and so are unlikely to be solely magnetic in origin. A subsequent scan, after the field is removed, Fig. 4(d), shows that the vortices have reformed but at different positions and with different geometries, showing that the vortex microstructure is not pinned, as expected for an easy plane ferromagnet. The more angular geometry of vortex cores, see the high-lighted square in Fig. 4(d), is associated with larger stray fields; this likely indicates that the microstructure, at 100 K, has not fully relaxed to the virgin state on the timescale of our measurements, tens of minutes.

In order to directly connect the images on vortex-domain microstructures to our bulk measurements, we use micromagnetic simulation. The micromagnetic parameters were determined based on the bulk magnetometry data and are used as input parameters to compute the mesoscale magnetic patterns, as shown in Fig. 4(e) (for details, see the supplementary material). Here, the small arrows and the color map represent the local orientation of the magnetization vector. The pattern is typical for an easy-plane magnet, with sets of vortex-antivortex pairs, one of which is highlighted in Fig. 4(f) showing the continuous in-plane rotation of the magnetization.

The calculated MFM signal for this magnetization pattern [Fig. 4(g)] is in good qualitative agreement with the observed zero-field states, e.g., Figs. 4(b) and 4(d), showing a series of vortex points connected by domain walls. The simulations also show that the contrast at the walls depends on the exact nature of the magnetization reorientation: Some walls have very sharp bright-dark features, while others have smoother transitions, again, as observed in the MFM data. Note that the in-plane closure domains with an MFM are well established for thin Permalloys films or thin flakes Van der Waals ferromagnets^{46,47} but is not common for bulk crystals with easy-plane magnetocrystalline anisotropy.

In conclusion, we have grown high-quality bulk single crystals of kagome bilayer ferromagnet Fe₃Sn and performed magnetization and MFM studies. The studies revealed a strong easy-plane anisotropy characterized by the first-order anisotropy constant $K_1 \approx -1.0 \times 10^6 \text{ J/m}^3$ at 300 K and $-1.3 \times 10^6 \text{ J/m}^3$ at 2 K. Three independent methods applied for the calculation of anisotropy constants in our work provide values that are in good agreement with each other. The DFT self-consistent computations reveal the easy-plane preferable magnetization direction and provide atom spin/orbital moments and

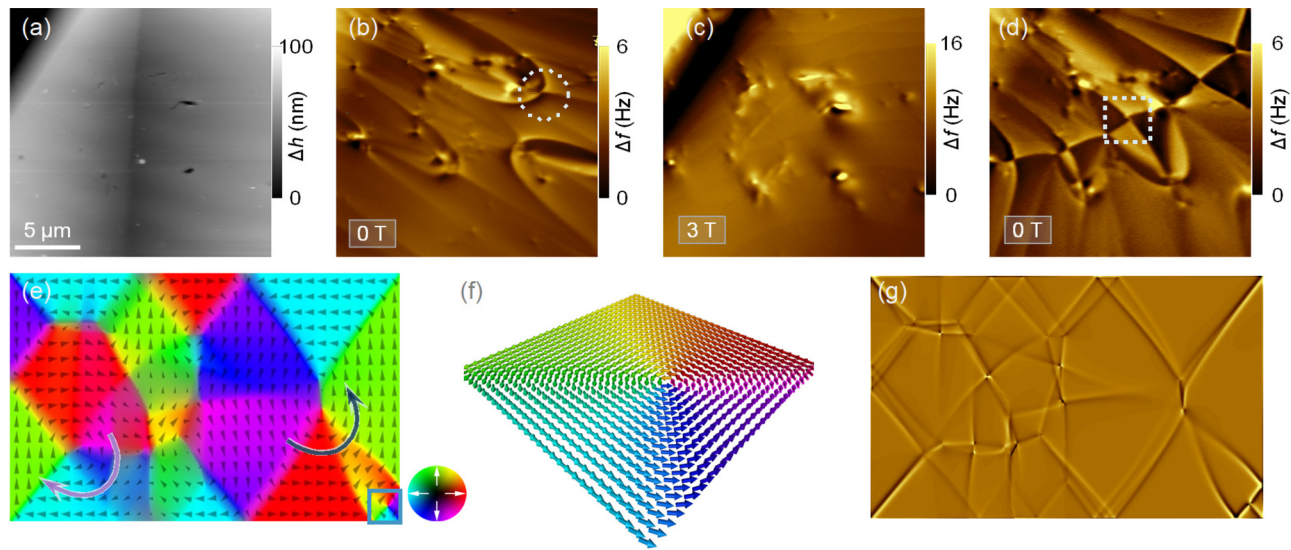


FIG. 4. (a) Topographic image collected in contact mode on an as-grown Fe_3Sn *ab* surface, also imaged in the MFM scans in panels (b), (c), and (d). (b)–(d) MFM images, recorded at 100 K, showing the shift in resonance frequency of the cantilever: Light/dark colors show an increase/decrease in the resonance frequency. (b) Extended domain walls meeting at vortex cores in the zero-field state. (c) Uniform MFM signal, observed except in the vicinity of topographic features, indicate uniform magnetization in 3 T. (d) The zero-field state after field treatment hosts a high density of vortices, some of which are much more angular in structure. The difference between the fully relaxed vortex structure (b) and the metastable structure shortly after the removal of a field (d) is highlighted by the dashed circle and square, respectively. (e) Micromagnetic simulations of the local orientation of the magnetization (gray arrows), viewed down the *c* axis. The false color code (bottom right) indicates the in-plane orientation of the magnetization vector. The clockwise and anticlockwise arrows stand for vortex–antivortex pairs. (f) Magnified view of one of the closure structures (vortices) in (e). (g) MFM response calculated for the domain pattern in panel (e).

MAE values consistent with the experiment. Our MFM study further confirms the system to be an easy-plane ferromagnet that contains a rich microstructure of the magnetization pattern dominated by (anti)-vortices. The experimentally observed MFM contrast is well reproduced by the micromagnetic simulations, using experimentally determined values of the magnetic interaction parameters. Overall, our bulk and microscopic experimental studies provide a reliable approach to quantify magnetic anisotropy and spin arrangement of the itinerant ferromagnet Fe_3Sn , which is an important step toward understanding complex magnetism emerging in kagome magnets.

See the supplementary material for details of experimental procedures, analytical and DFT calculation, and single-crystal XRD refinement.

This work was supported by the Deutsche Forschungsgemeinschaft (DFG, German Research Foundation) TRR 360-492547816 and Project No. ANCD 20.80009.5007.19 (Moldova). D.M.E. acknowledges the funding by the DFG individual fellowship (No. EV 305/1-1). S.M.G. acknowledges funding and the computational resources by the U.S. Department of Energy under Contract No. DEAC02-05-CH11231.

AUTHOR DECLARATIONS

Conflict of Interest

The authors have no conflicts to disclose.

Author Contributions

Lilian Prodan: Conceptualization (equal); Formal analysis (equal); Investigation (equal); Writing – original draft (equal); Writing –

review & editing (equal). **Vladimir Tsurkan:** Conceptualization (lead); Formal analysis (lead); Writing – original draft (lead); Writing – review & editing (equal). **Istvan Kézsmárki:** Conceptualization (equal); Funding acquisition (lead); Supervision (lead); Writing – review & editing (equal). **Donald Malcolm Evans:** Investigation (equal); Writing – review & editing (equal). **Sinead M. Griffin:** Formal analysis (equal); Writing – review & editing (equal). **Andreas Ostlin:** Formal analysis (equal); Writing – review & editing (equal). **Markus Althaler:** Investigation (equal); Writing – review & editing (equal). **Erik Lysne:** Formal analysis (equal). **Irina Filippova:** Formal analysis (equal); Investigation (equal). **Sergiu Shova:** Investigation (equal). **Liviu Chioncel:** Conceptualization (equal); Formal analysis (equal); Writing – review & editing (equal).

DATA AVAILABILITY

The data that support the findings of this study are available from the corresponding author upon reasonable request.

REFERENCES

- ¹I. Mazin, H. Jeschke, F. Lechermann, H. Lee, M. Fink, R. Thomale, and R. Valenti, *Nat. Commun.* **5**, 4261 (2014).
- ²L. Ye, M. Kang, J. Liu, F. von Cube, C. R. Wicker, T. Suzuki, C. Jozwiak, A. Bostwick, E. Rotenberg, D. C. Bell, L. Fu, R. Comin, and J. G. Checkelsky, *Nature* **555**, 638–642 (2018).
- ³A. Bolens and N. Nagaosa, *Phys. Rev. B* **99**, 165141 (2019).
- ⁴J. Yin, S. S. Zhang, G. Chang, Q. Wang, S. S. Tsirkin, Z. Guguchia, B. Lian, H. Zhou, K. Jiang, I. Belopolski, N. Shumiya, D. Multer, M. Litskevich, T. A. Cochran, H. Lin, Z. Wang, T. Neupert, S. Jia, H. Lei, and M. Z. Hasan, *Nat. Phys.* **15**, 443–448 (2019).

- ⁵M. Kang, L. Ye, S. Fang, J.-S. You, A. Levitan, M. Han, J. I. Facio, C. Jozwiak, A. Bostwick, E. Rotenberg, M. K. Chan, R. D. McDonald, D. Graf, K. Kaznatcheev, E. Vescovo, D. C. Bell, E. Kaxiras, J. van den Brink, M. Richter, M. Prasad Ghimire, J. G. Checkelsky, and R. Comin, *Nat. Mater.* **19**, 163–169 (2020).
- ⁶T. Chen, T. Tomita, S. Minami, M. Fu, T. Koretsune, M. Kitatani, I. Muhammad, D. Nishio-Hamane, R. Ishii, F. Ishii, R. Arita, and S. Nakatsuji, *Nat. Commun.* **12**, 572 (2021).
- ⁷S. Nakatsuji, N. Kiyohara, and T. Higo, *Nature* **527**, 212–215 (2015).
- ⁸Z. Hou, W. Ren, B. Ding, G. Xu, Y. Wang, B. Yang, Q. Zhang, Y. Zhang, E. Liu, F. Xu, W. Wang, G. Wu, X. Zhang, B. Shen, and Z. Zhang, *Adv. Mater.* **29**, 1701144 (2017).
- ⁹W. Ma, X. Xu, J.-X. Yin, H. Yang, H. Zhou, Z.-J. Cheng, Y. Huang, Z. Qu, F. Wang, M. Z. Hasan, and S. Jia, *Phys. Rev. Lett.* **126**, 246602 (2021).
- ¹⁰E. Liu, Y. Sun, N. Kumar, L. Muechler, A. Sun, L. Jiao, S.-Y. Yang, D. Liu, A. Liang, Q. Xu, J. Kroder, V. Süß, H. Borrmann, C. Shekhar, Z. Wang, C. Xi, W. Wang, W. Schnelle, S. Wirth, Y. Chen, S. T. B. Goennenwein, and C. Felser, *Nat. Phys.* **14**, 1125–1131 (2018).
- ¹¹S. N. Guin, P. Vir, Y. Zhang, N. Kumar, S. J. Watzman, C. Fu, E. Liu, K. Manna, W. Schnelle, J. Gooth, C. Shekhar, Y. Sun, and C. Felser, *Adv. Mater.* **31**, 1806622 (2019).
- ¹²S.-Y. Yang, Y. Wang, B. R. Ortiz, D. Liu, J. Gayles, E. Derunova, R. Gonzalez-Hernandez, L. Šmejkal, Y. Chen, S. P. Parkin, S. D. Wilson, E. S. Toberer, T. McQueen, and M. N. Ali, *Sci. Adv.* **6**, eabb6003 (2020).
- ¹³B. R. Ortiz, S. M. Teicher, Y. Hu, J. L. Zuo, P. M. Sarte, E. C. Schueller, A. M. Abeykoon, M. J. Krogstad, S. Rosenkranz, R. Osborn, R. Seshadri, L. Balents, J. He, and S. D. Wilson, *Phys. Rev. Lett.* **125**, 247002 (2020).
- ¹⁴T. Chen, S. Minami, A. Sakai, Y. Wang, Z. Feng, T. Nomoto, M. Hirayama, R. Ishii, T. Koretsune, R. Arita, and S. Nakatsuji, *Sci. Adv.* **8**, eabk1480 (2022).
- ¹⁵Z. Lin, J.-H. Choi, Q. Zhang, W. Qin, S. Yi, P. Wang, L. Li, Y. Wang, H. Zhang, Z. Sun, L. Wei, S. Zhang, T. Guo, Q. Lu, J.-H. Cho, C. Zeng, and Z. Zhang, *Phys. Rev. Lett.* **121**, 096401 (2018).
- ¹⁶H. Zhang, H. Feng, X. Xu, W. Hao, and Y. Du, *Adv. Quantum Technol.* **4**, 2100073 (2021).
- ¹⁷J. Watanabe, Y. Araki, K. Kobayashi, A. Ozawa, and K. Nomura, *J. Phys. Soc. Jpn.* **91**, 083702 (2022).
- ¹⁸A. Bogdanov and D. Yablonskii, *Sov. Phys. Solid State* **22**, 399–403 (1980).
- ¹⁹X. Yu, M. Mostovoy, Y. Tokunaga, W. Zhang, K. Kimoto, Y. Matsui, Y. Kaneko, N. Nagaosa, and Y. Tokura, *Proc. Natl. Acad. Sci. U. S. A.* **109**, 8856–8860 (2012).
- ²⁰T. Okubo, S. Chung, and H. Kawamura, *Phys. Rev. Lett.* **108**, 017206 (2012).
- ²¹S. A. Montoya, S. Couture, J. J. Chess, J. C. T. Lee, N. Kent, D. Henze, S. K. Sinha, M.-Y. Im, S. D. Kevan, P. Fischer, B. J. McMorran, V. Lomakin, S. Roy, and E. E. Fullerton, *Phys. Rev. B* **95**, 024415 (2017).
- ²²J. Tang, L. Kong, Y. Wu, W. Wang, Y. Chen, Y. Wang, J. Li, Y. Soh, Y. Xiong, M. Tian, and H. Du, *ACS Nano* **14**, 10986–10992 (2020).
- ²³M. Preißinger, K. Karube, D. Ehlers, B. Szigeti, H.-A. K. von Nidda, J. S. White, V. Ukleev, H. M. Rønnow, Y. Tokunaga, A. Kikkawa, Y. Tokura, Y. Taguchi, and I. Kézsmárki, *npj Quantum Mater.* **6**, 70 (2021).
- ²⁴M. Althaler, E. Lysne, E. Roede, L. Prodan, V. Tsurkan, M. A. Kassem, H. Nakamura, S. Krohns, I. Kézsmárki, and D. Meier, *Phys. Rev. Res.* **3**, 043191 (2021).
- ²⁵X. Yu, Y. Tokunaga, Y. Taguchi, and Y. Tokura, *Adv. Mater.* **29**, 1603958 (2017).
- ²⁶M. E. Gouva, G. M. Wysin, A. R. Bishop, and F. G. Mertens, *Phys. Rev. B* **39**, 11840–11849 (1989).
- ²⁷K. Shiget, T. Okuno, K. Mibu, T. Shinjo, and T. Ono, *Appl. Phys. Lett.* **80**, 4190–4192 (2002).
- ²⁸F. P. Chmiel, N. W. Price, R. D. Johnson, A. D. Lamirand, J. Schad, G. van der Laan, D. T. Harris, J. Irwin, M. S. Rzchowski, C.-B. Eom, and P. G. Radaelli, *Nat. Mater.* **17**, 581–585 (2018).
- ²⁹N. Gao, S. G. Je, M. Y. Im, J. W. Choi, M. Yang, Q. Li, T. Y. Wang, S. Lee, H. S. Han, K. S. Lee, W. Chao, C. Hwang, J. Li, and Z. Q. Qiu, *Nat. Commun.* **10**, 5603 (2019).
- ³⁰X. Zhang, Y. Zhou, K. M. Song, T.-E. Park, J. Xia, M. Ezawa, X. Liu, W. Zhao, G. Zhao, and S. Woo, *J. Phys.: Condens. Matter* **32**, 143001 (2020).
- ³¹H. Giefers and M. Nicol, *J. Alloys Compd.* **422**, 132–144 (2006).
- ³²L. Häggström, T. Ericsson, R. Wäppling, and K. Chandra, *Phys. Scr.* **11**, 47 (1975).
- ³³B. C. Sales, J. Yan, W. R. Meier, A. D. Christianson, S. Okamoto, and M. A. McGuire, *Phys. Rev. Mater.* **3**, 114203 (2019).
- ³⁴G. L. Caër, B. Malaman, and B. Roques, *J. Phys. F* **8**, 323 (1978).
- ³⁵G. Trumphy, E. Both, C. Djéga-Mariadassou, and P. Lecocq, *Phys. Rev. B* **2**, 3477–3490 (1970).
- ³⁶S. Kulshreshtha and P. Raj, *J. Phys. F: Met. Phys.* **11**, 281 (1981).
- ³⁷K. Heritage, B. Bryant, L. A. Fenner, A. S. Wills, G. Aepli, and Y.-A. Soh, *Adv. Funct. Mater.* **30**, 1909163 (2020).
- ³⁸G. He, L. Peis, R. Stumberger, L. Prodan, V. Tsurkan, N. Unglert, L. Chioncel, I. Kézsmárki, and R. Hackl, *Phys. Status Solidi B* **259**, 2100169 (2022).
- ³⁹C. Djéga-Mariadassou, P. Lecocq, G. Trumphy, J. Träff, and P. Ostergaard, *Il Nuovo Cimento B* **46**, 35 (1966).
- ⁴⁰B. C. Sales, B. Sagarov, M. A. McGuire, D. J. Singh, and D. S. Parker, *Sci. Rep.* **4**, 7024 (2014).
- ⁴¹B. Fayyazi, K. P. Skokov, T. Faske, I. Opahle, M. Duerrschabel, T. Helbig, I. Soldatov, U. Rohrmann, L. Molina-Luna, K. Gueth *et al.*, *Acta Mater.* **180**, 126–140 (2019).
- ⁴²B. D. Cullity and C. D. Graham, *Introduction to Magnetic Materials*, 2nd ed., (IEEE Press, John Wiley and Sons, 2009).
- ⁴³W. Sucksmith and J. E. Thompson, *Proc. R. Soc. London, Ser. A* **225**, 362–375 (1954).
- ⁴⁴J. Alameda, J. Deportes, D. Givord, R. Lemaire, and Q. Lu, *J. Magn. Magn. Mater.* **15–18**, 1257–1258 (1980).
- ⁴⁵A. S. Bolyachkin, D. S. Neznakhin, and M. I. Bartashevich, *J. Appl. Phys.* **118**, 213902 (2015).
- ⁴⁶H. J. Mamin, D. Rugar, J. E. Stern, R. E. Fontana, and P. Kasiraj, *Appl. Phys. Lett.* **55**, 318–320 (1989).
- ⁴⁷A. Purbawati, J. Coraux, J. Vogel, A. Hadj-Azzem, N. Wu, N. Bendiab, D. Jegouso, J. Renard, L. Marty, V. Bouchiat, A. Sulpice, L. Aballe, M. Foerster, F. Genuzio, A. Locatelli, T. O. Mente, Z. V. Han, X. Sun, M. Nez-Regueiro, and N. Rougemaille, *ACS Appl. Mater. Interfaces* **12**, 30702–30710 (2020).